RESEARCH ARTICLE
doi: 10.2306/scienceasia1513-1874.2025.s024

ScienceAsia 51S (2): 2025: ID 2025s024: **1–9**

Phase characterization of amorphous tin oxides micro/nanoparticles by Raman spectroscopy

Suparoek Yarin[a], **Siripatsorn Thanasanvorakun**[a], **Vasan Yarangsi**[a], **Kritsada Hongsith**[a,b], **Wakul Bumrungsan**[a,b], **Sukrit Sucharitakul**[a], **Surachet Phadungdhitidhada**[a], **Supab Choopun**[a,*]

[a] Department of Physics and Materials Science, Faculty of Science, Chiang Mai 50200 Thailand
[b] Office of Research Administration, Chiang Mai University, Chiang Mai 50200 Thailand

[*]Corresponding author, e-mail: supab99@gmail.com

Received 30 Nov 2024, Accepted 10 Nov 2025
Available online 20 Dec 2025

ABSTRACT: Raman spectroscopy is a valuable technique for elucidating the phase evolution of mixed-phase amorphous tin oxides, which is challenging to characterize due to its complex and low-crystalline structure. In this work, the mixed phase of amorphous tin oxides was synthesized via the electrochemical process. The as-prepared tin oxides were annealed at temperatures ranging from 100 to 500 °C in both nitrogen (N_2) and air environments. The properties of the tin oxides were investigated using X-ray diffraction (XRD), Raman spectroscopy, scanning electron microscopy (SEM), X-ray photoelectron spectroscopy (XPS), and photoluminescence (PL) spectroscopy. From the results, the XRD patterns exhibited broad and silent peaks, especially at temperatures below 200 °C in both environments, which limit the detection of phase evolution. Moreover, XPS mainly provided information on chemical states rather than the amorphous phase. In contrast, the Raman spectroscopy effectively identified vibration modes of the tin oxide phases, providing direct insights into phase transformations, local bonding, and defects, even in low-crystalline systems. The results revealed that under a sufficient ambient oxygen, amorphous SnO_2/SnO micro/nanoparticles completely transformed to Sn_2O_3/Sn_3O_4 and SnO_2 at 500 °C. However, the annealing at 500 °C under ambient N_2 resulted in the formation of SnO combined with Sn_2O_3, Sn_3O_4, and SnO_2. These findings highlighted that the Raman spectroscopy technique is a crucial procedure for revealing the phase of amorphous tin micro/nanoparticle oxides, providing unique and complementary information on phase evolution and defect structure, which is critical for selecting the appropriate tin oxide phases for p–n junction device applications.

KEYWORDS: phase characterization, Raman spectroscopy, amorphous tin oxides, nano/microparticles

INTRODUCTION

Tin oxides (SnO_2 and SnO) micro and nanoparticles are attractive semiconductors because of their unique properties. SnO_2 exhibits n-type semiconducting properties with a wide band gap of 3.6 eV and high transparency in the UV and visible spectrum range [1]. However, SnO exhibits p-type semiconducting properties with an optical bandgap of ∼2.7–3.2 eV and a metastable phase in an oxygen-rich environment [2]. Therefore, tin oxides have various potential applications, including antibacterial agents, photocatalytic agents, gas sensors, and perovskite solar cells [3, 4]. Moreover, the formation of p–n heterojunctions and the bandgap engineering of hybrid tin oxides (n-SnO_2 and p-SnO) are useful in several applications, such as photocatalytic agents, gas sensors, and lithium-ion batteries [5, 6].

Amorphous tin oxides have become a promising alternative material due to their numerous advantages, such as low-cost production, low synthesis temperature, and compatibility with flexible substrates. These advantages are suitable for various applications. For example, the thin films of amorphous SnO_2 have been used in perovskite solar cells and show comparable stability and power conversion efficiency (PCE) [7]. However, synthesis, phase characterization, and phase transformation of the amorphous mixed-phase p and n-type tin oxide micro/nanoparticles have been rarely reported due to the complex and disordered structure of the material, including many oxidation states and vacancies.

Phase characterizations of tin oxides are important for understanding their physical properties and exploring potential applications. However, phase characterization and evolution of amorphous tin oxides are challenging using conventional techniques, such as X-ray diffraction (XRD), due to the typically weak and broad peaks of amorphous signals, which makes them challenging to identify. Moreover, X-ray photoelectron spectrometry (XPS) was utilized by Wang et al for the phase components analysis of the SnO_2, Sn^{2+}/SnO_2, SnO-SnO_2, and SnO [8]. Variations of oxidation state were used to identify the phases of the samples. However, XPS primarily reveals the chemical states rather than the amorphous phase. Moreover, XPS exhibits long-time sample preparation, and the samples must be analyzed in a vacuum.

From these drawbacks, Raman spectroscopy is an outstanding analytical technique for amorphous material characterization because of the simplicity of the sample preparation, short-time characterization, and non-destructive analysis of the samples, including the detection of molecular vibrations that potentially

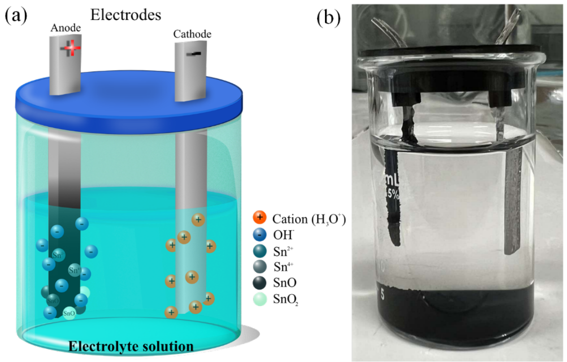

Fig. 1 (a) Schematic diagram and (b) a photograph of the electrochemical system for preparation of amorphous tin micro/nanoparticles.

demonstrate chemical components of the amorphous materials [9–12]. Importantly, Raman spectroscopy can reveal subtle phase transformations that XRD or XPS do not clearly detect. Raman spectroscopy was employed by Guillen and Herrero to investigate the phase of p-type SnO thin films under different oxygen partial pressures (O_{pp}) ranging from 9 to 24%. The optimum SnO phase was observed at 12% O_{pp}. The phase transitions were further examined by heating the thin films from 200 °C to 500 °C in ambient air. At 400 °C, this demonstrates the excellent capability of Raman spectroscopy to identify material phases [10].

Therefore, the aim of the present study is to characterize the phase evolution of the mixed-phase amorphous tin oxide micro and nanoparticles using a low-temperature electrochemical technique. Morphology, phase, crystallinity properties, and elements of the as-prepared sample are investigated using scanning electron microscopy (SEM), XRD, Raman spectroscopy, and XPS. The morphology of the amorphous formation mechanism is summarized and described in terms of chemical reactions. Furthermore, the phase and phase evolution of amorphous tin oxides at different temperatures in rich and poor oxygen environments are also investigated in-depth using Raman spectroscopy, including the conventional techniques by XRD and photoluminescence spectroscopy (PL).

MATERIALS AND METHODS

Synthesis and study of the phase evolution of amorphous tin oxide micro/nanoparticles

Amorphous tin micro/nanoparticles were prepared by an electrochemical process, as shown in a schematic diagram and a photograph in Fig. 1(a,b). The tin foil electrodes (5 mm × 50 mm × 2 mm, 99.99%, MAGERIAL, China) were cleaned with acetone, isopropyl alcohol (IPA), and ethanol for 30 min each to remove impurities and contamination from the electrodes. The electrodes were immersed in a 0.1 M citric acid electrolyte solution. The 6 V voltage was applied to the electrodes by a DC power supply (DP831A, RIGOL Technologies, Beijing, China) for 48 h. The bottom sediments were collected and cleaned with deionized water several times. Finally, the precipitates were dried on a hot plate at 50 °C for 3 h. To study the phase evolution of the amorphous tin oxides, the as-prepared amorphous tin oxides were annealed from 100 °C to 500 °C in an air-ambient and nitrogen (N_2) gas environment.

Characterizations

The morphology of the as-prepared amorphous tin oxides was investigated using SEM (JSM-IT800, JEOL Ltd., Tokyo, Japan). The elemental ratio of the as-synthesized tin oxide sample was determined by XPS (Axis Ultra DLD, Kratos Analytical Ltd., Manchester, UK). To demonstrate the structure, phase, and phase evolution, the amorphous tin oxides were characterized by XRD with Cu Kα X-ray radiation source (Miniflex II diffractometer, Rigaku Corp., Tokyo, Japan) and Raman spectrometer (LabRAM HR Evolution, HORIBA Scientific, Paris, France) with 1% intensity power of 532 nm laser source for preventing the phase changing during measurement, as shown in Fig. S1 and Fig. S2, and investigation by taking acquisition time for 60 s. Moreover, the luminescence of tin oxide powder was investigated by photoluminescence with a 345 nm laser.

RESULTS AND DISCUSSION

Analysis of as-prepared amorphous tin oxide micro/nanoparticles

Fig. 1 depicts the electrochemical process using tin foils in citric acid solutions at 6 V for 48 h. In the electrochemical process, gas bubbles formed at the anode and cathode electrodes, indicating the reaction between the tin foil and the solution. The color of the anode changed to black after 15 min, whereas the color of the cathode remained unchanged. The sediment was observed at the bottom of the electrodes after processing for 3 h. Fig. 2(a,b) shows the magnification images of the as-synthesized tin oxide powder. The size of the particles indicated a wide range from micro to nano sizes. The tin oxide morphology exhibited a unique porous surface formed by randomly pulling tin ions out of the anode electrode under an electric field and reacting with solution ions during the electrochemical process. XRD pattern of the as-prepared powder is shown in Fig. 2(c) for the analysis of the phase and crystallinity property. The broad peak observed in the XRD pattern confirms the amorphous nature of the as-prepared powder. This material lacks the long-range crystalline order that prevents the formation of sharp diffraction peaks, resulting in a pattern that does not match the diffraction pattern of crystalline SnO or SnO_2. This broad characteristic is consistent with

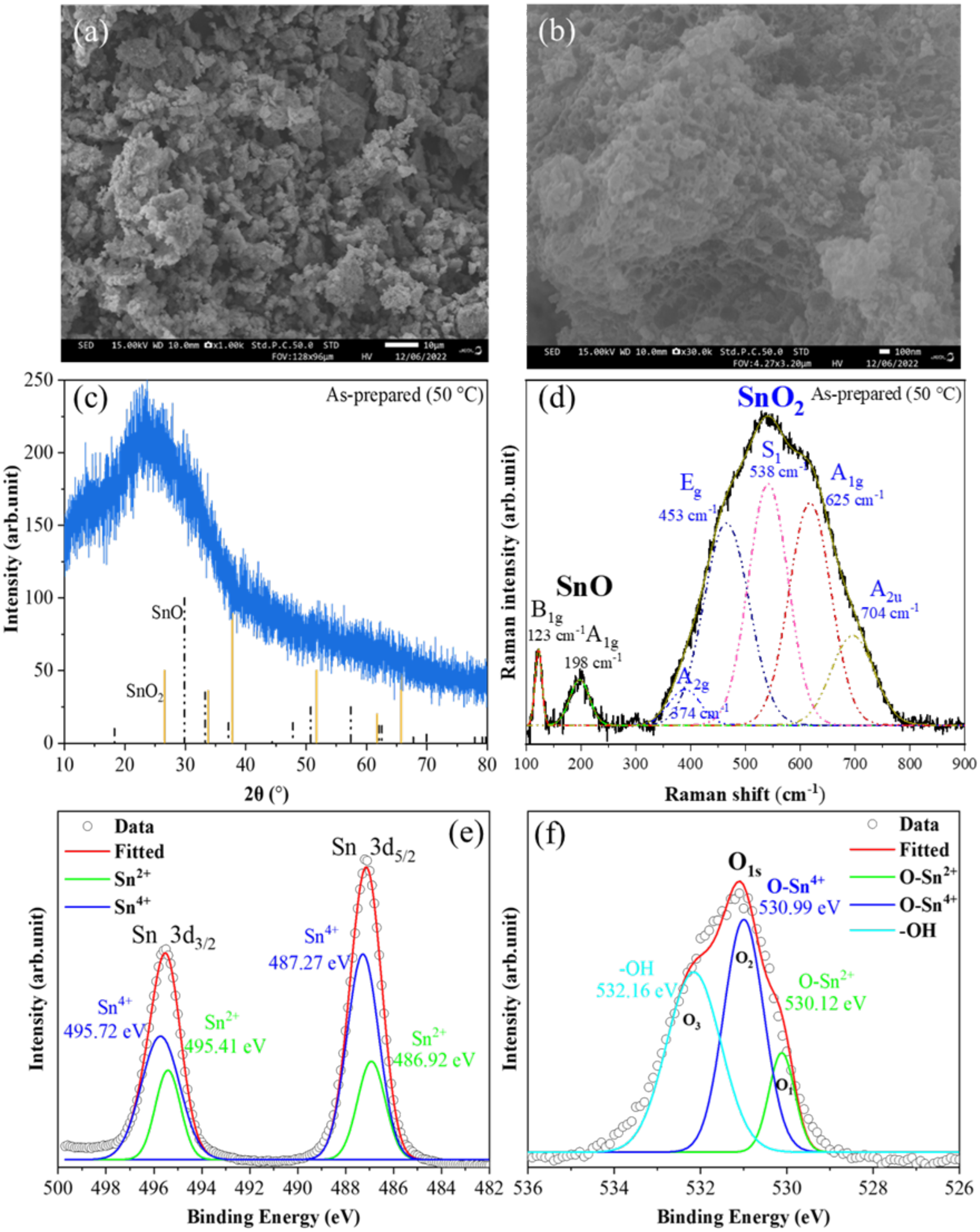

Fig. 2 (a,b) SEM images, (c) XRD pattern, (d) Raman spectrum, and (e,f) XPS spectrum of as-prepared amorphous tin oxides powder.

amorphous tin oxides and other metal oxide systems [13, 14].

The phase of the as-prepared tin oxides was demonstrated by detecting the vibration modes of tin oxides from Raman spectroscopy, as shown in Fig. 2(d). The Raman signals were observed in the center of the peaks around ∼123 cm^{-1} and 200 cm^{-1}, correlated with the characteristic B_{1g} and A_{1g} [10, 15, 16] vibration modes of the typical SnO phase. The Raman signal exhibited a broad peak ranging from 370 to 800 cm^{-1}. The broader peak was deconvoluted into five peaks at the center around 374, 453, 538, 625, and 704 cm^{-1}, which could be attributed to the A_{2g}, E_g, S_1, A_{1g}, and A_{2u} vibration modes of the SnO_2 phase

[17–19]. The peaks at around 570 cm^{-1} (S_1) could not be observed in general in the SnO_2 because it was related to the presence of oxygen vacancies, hydroxyl group, surface disorder, or amorphous attribute of SnO_2 [9,20,21]. Therefore, the presence of SnO and SnO_2 vibration modes showed that the as-prepared tin oxides were an amorphous mixed phase of SnO and SnO_2.

The XPS technique was used to characterize the as-prepared powder to investigate the chemical components. Fig. 2(e) shows the Sn $3d_{5/2}$ and Sn $3d_{3/2}$ peaks from XPS spectra. The peaks of the Sn $3d_{5/2}$ and Sn $3d_{3/2}$ were deconvoluted into four peaks. The 486.92 eV and 495.41 eV peaks were related to the SnO phase, and the peaks at 487.27 eV and 495.72 eV corresponded with the SnO_2 phase. Fig. 2(f) shows the O_{1s} XPS spectrum of the tin oxide powder, which exhibited three peaks: 530.12 eV (O_1), 530.99 eV (O_2), and 532.16 eV (O_3). The distinctive O_2 peak corresponded to the oxygen species that were combined with the Sn^{4+} in SnO_2. The O_1 peak was assigned to the oxygen in SnO, and the O_3 was related to the hydroxyl group (OH^-) [22,23] with oxygen vacancies on the surface of the tin oxide sample. The height of the O_3 intensity was comparable to the O_1 peak, confirming that the as-prepared mixed-phases of tin oxides combined with the hydroxyl groups. These hydroxyl groups resulted in a disordered structure of the tin oxide, leading to the presence of amorphous properties in the samples.

Growth mechanisms of an amorphous tin oxide micro/nanoparticles

The growth mechanisms of amorphous tin oxide micro/nanoparticles can be represented by the following chemical reaction. First, the gas bubbles at the cathode and anode electrodes, when a 6 V voltage was applied to the electrodes with current from the power supply, can be described by the following Eqs. (1) and (2). Meanwhile, the ions of Sn^{2+} and Sn^{4+} were generated at the tin anode electrodes, as shown in Eqs. (3) and (4). For the evaluation of the spontaneity of these processes, the standard reduction and oxidation potential (E^0) [24,25] were used to calculate the overall reaction potential ($E^0{}_{cell}$) as presented in Eqs. (5) and (6). For both reactions, the negative standard cell potential indicates that the reactions were non-spontaneous in the absence of an applied voltage. However, in our work, we applied a 6 V voltage to the electrodes, which is higher than the $E^0{}_{cell}$. That led to these following reactions. The ions of Sn^{2+} and Sn^{4+} further reacted with the hydroxyl group in an electrolyte solution to form SnO and SnO_2, as presented in the dehydration reaction Eqs. (7) and (8) [8,26].

Cathode (Reduction):

$$2\,H_2O_{(l)} + 2\,e^- \longrightarrow 2\,OH^-_{(aq)} + H_{2(g)} \quad (E^0) = -0.83\text{ V} \tag{1}$$

Anode (Oxidation):

$$2\,H_2O_{(l)} \longrightarrow 4\,H^+_{(aq)} + O_{2(g)} + 4\,e^- \quad (E^0) = -1.23\text{ V} \tag{2}$$

Electrolyte (Oxidation):

$$Sn_{(s)} \longrightarrow Sn^{2+}_{(aq)} + 2\,e^- \qquad (E^0) = +0.14\text{ V} \tag{3}$$

$$Sn_{(s)} \longrightarrow Sn^{4+}_{(aq)} + 4\,e^- \qquad (E^0) = -0.005\text{ V} \tag{4}$$

Overall cell reduction and oxidation reactions:

$$2\,H_2O_{(l)} + Sn_{(s)} \longrightarrow Sn^{2+}_{(aq)} + 2\,OH^-_{(aq)} + H_{2(g)} \qquad E^0_{cell} = -0.690\text{ V} \tag{5}$$

$$4\,H_2O_{(l)} + Sn_{(s)} \longrightarrow Sn^{4+}_{(aq)} + 4\,OH^-_{(aq)} + 2\,H_{2(g)} \qquad E^0_{cell} = -0.835\text{ V} \tag{6}$$

Dehydration reactions:

$$Sn^{2+}_{(aq)} + 2\,OH^-_{(aq)} \longrightarrow SnO_{(s)} + H_2O_{(l)} \tag{7}$$

$$Sn^{4+}_{(aq)} + 4\,OH^-_{(aq)} \longrightarrow SnO_{2(s)} + 2\,H_2O_{(l)} \tag{8}$$

Acid-base dissociation of citric acid:

$$C_6H_8O_{7(aq)} + 3\,H_2O_{(l)} \longleftrightarrow C_6H_5O^{3-}_{7(aq)} + 3\,H_3O^+_{(aq)} \tag{9}$$

Moreover, the citric acid ($C_6H_8O_7$) in electrolyte solution could be split into three hydrogen ions (H_3O^+) as described in acid-base dissociation as Eq. (9). These hydrogen ions and the hydroxyl group in the solution could disorder the crystalline formation of tin oxides due to the hydrogenation and doping in the tin oxides structure [27–29], leading to asymmetric properties and amorphous attributes of as-prepared tin oxides.

Phase evolution analysis on amorphous tin oxide micro/nanoparticles

To further study the effects of temperature and oxygen conditions on the mixed phase amorphous tin oxide, the amorphous tin oxide was annealed from 100 °C to 500 °C in air and the N_2 environment. Fig. 3(a,b) shows the colors and the XRD spectra of the mixed phase of tin oxides on the annealing temperature dependence in air and ambient N_2. The XRD pattern of the powder in both conditions, between 100 °C and 200 °C, exhibited broad and low-intensity patterns, indicating the amorphous characteristic of the powders. When the annealing temperature exceeded 300 °C, small diffraction peaks corresponding to the plane of rutile tetragonal SnO_2 became apparent. The crystallite sizes of the powder under both air and N_2 conditions were calculated using the Scherrer equation and are summarized in Table S1.

$$D = \frac{k\lambda}{\beta\cos\theta} \tag{10}$$

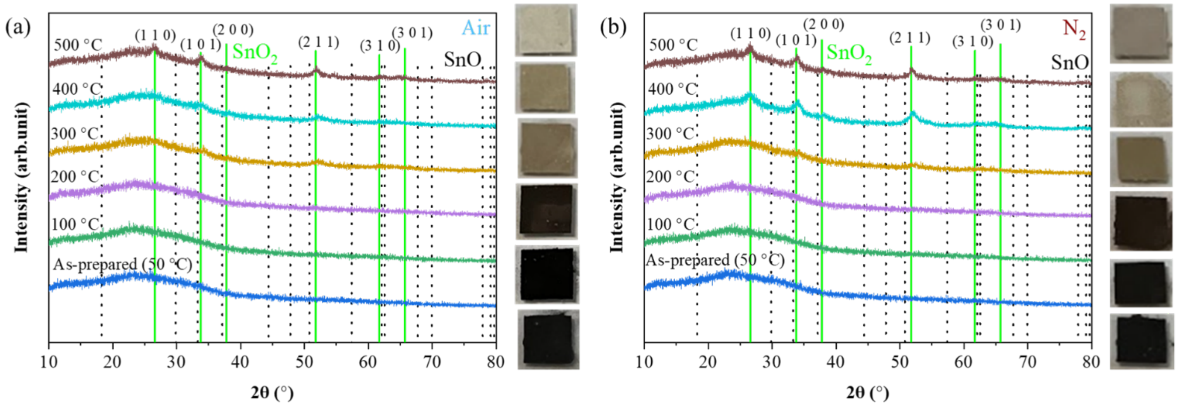

Fig. 3 XRD patterns of tin oxide micro/nanoparticles at different annealing temperatures in (a) air and (b) N_2 environments.

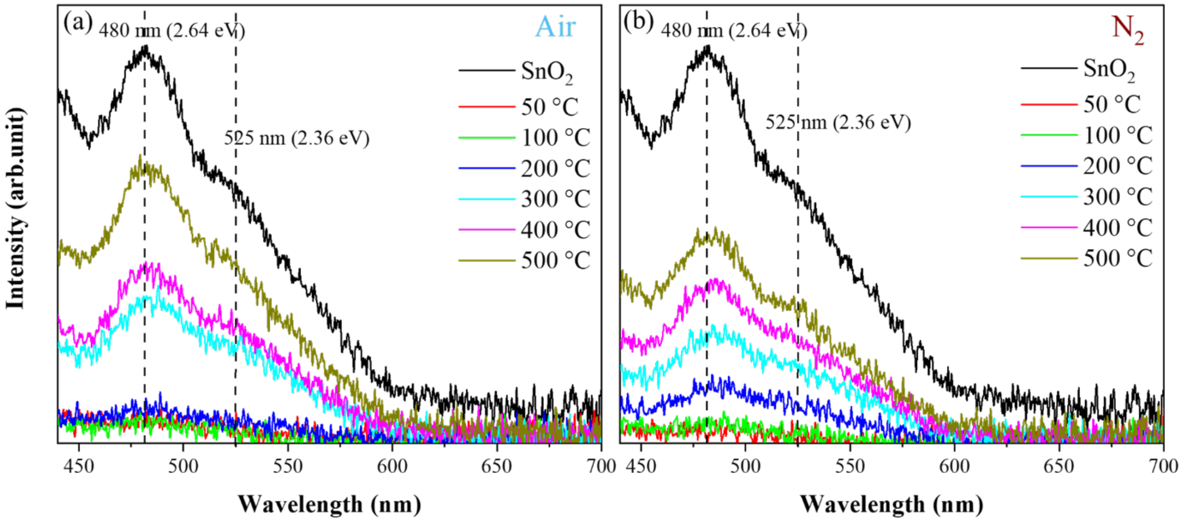

Fig. 4 Photoluminescence spectra of tin oxides micro/nanoparticles at different annealing temperatures in (a) air and (b) N_2 environments.

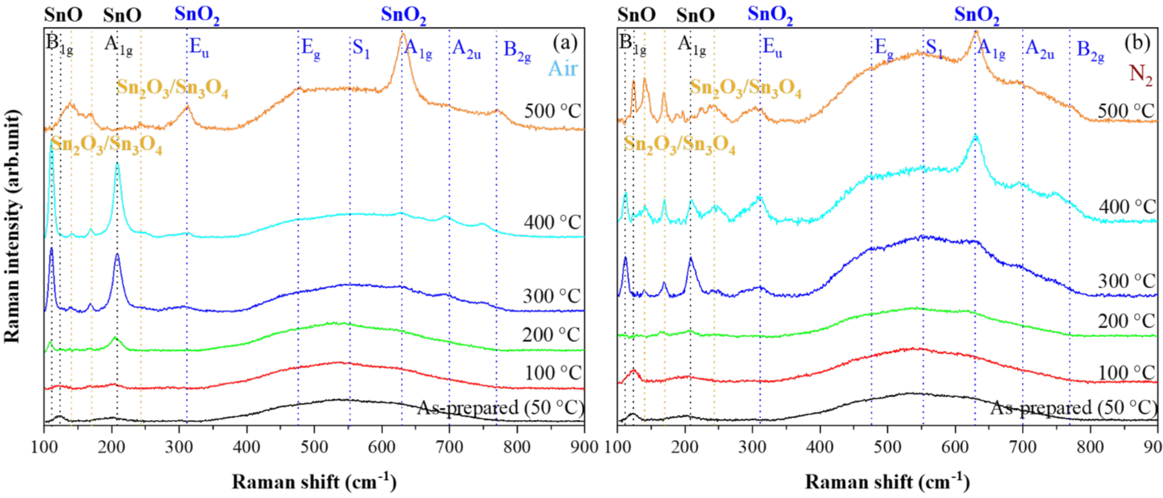

Fig. 5 Raman spectra of tin oxides at different temperatures in (a) air and (b) N_2 environments.

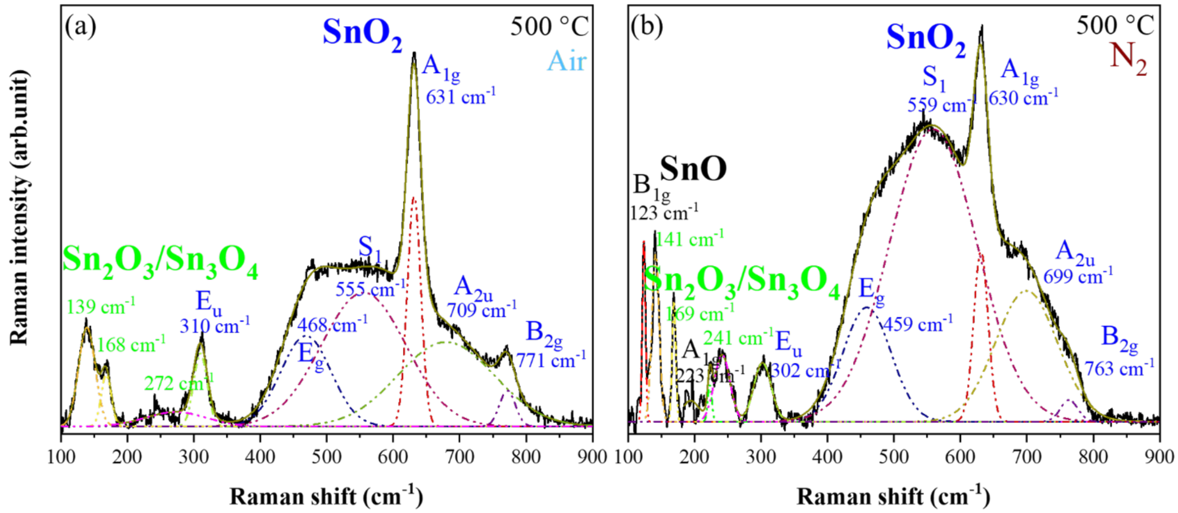

Fig. 6 Raman spectra of tin oxide at annealing temperatures of 500 °C in (a) air and (b) N_2 environments.

Table 1 Phases evolution of tin oxides micro/nanoparticles at different annealing temperatures in air and N_2 environments.

Air		N_2	
Temperature (°C)	Phases	Temperature (°C)	Phases
100	$SnO + SnO_2$	100	$SnO + SnO_2$
200	$SnO + SnO_2$	200	$SnO + Sn_3O_4 + Sn_2O_3 + SnO_2$
300	$SnO + Sn_3O_4 + Sn_2O_3 + SnO_2$	300	$SnO + Sn_3O_4 + Sn_2O_3 + SnO_2$
400	$SnO + Sn_3O_4 + Sn_2O_3 + SnO_2$	400	$SnO + Sn_3O_4 + Sn_2O_3 + SnO_2$
500	$Sn_3O_4 + Sn_2O_3 + SnO_2$	500	$SnO + Sn_3O_4 + Sn_2O_3 + SnO_2$

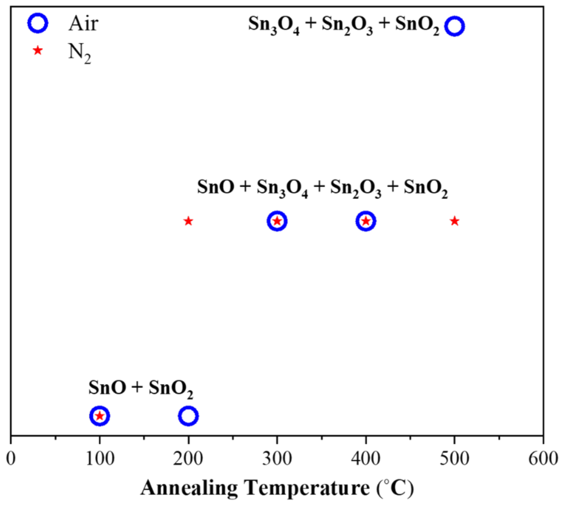

Fig. 7 Phase evolution of tin oxides at various temperatures in the air and N_2 environments.

where D is the average crystalline size, k is the Scherrer constant (0.94), λ is the X-ray wavelength (0.154 nm for Cu Kα), β is the full width at half maximum (FWHM), and θ is the Bragg angle (one half of the diffraction angle position 2θ (°)) [30]. The results showed that the crystallite size of the (211) plane increased with annealing temperature from 3.95 nm (air) and 4.71 nm (N_2) at 300 °C to 9.31 nm (air) and 9.99 nm (N_2) at 500 °C. The increase in crystallite size indicated the enhanced crystallinity and the transformation of amorphous tin oxides into crystalline SnO_2 with increasing annealing temperature.

The annealed powder from 100 °C to 200 °C in air and ambient N_2 showed a black color, which occurred from the presence of the SnO and hydrogenated SnO_2. The annealing of the powder at 300 °C to 400 °C exhibited a color change to a white-brown color, indicating a phase change to other phases, such as Sn_2O_3 and Sn_3O_4. Raman spectra confirmed this observation by showing peaks at ~140, 169 cm^{-1} (Fig. S3 and Fig. S4), which were consistent with the reported vibrational modes of the intermediate phases of Sn_2O_3 and Sn_3O_4 [31, 32]. Moreover, the 500 °C sample in the air environment exhibited an ivory-white color, which matches the color of pure SnO_2, as supported by the appearance of the strong A_{1g} (~633 cm^{-1}) Raman modes. In contrast, the 500 °C sample in the N_2 environment showed a grey-white color, and the Raman spectra still displayed residual peaks of SnO phases, indicating the powder could not transform into the high oxygen state of tin oxides under oxygen-deficient conditions.

The number of bonding species and crystalline symmetry affect the photoluminescenc (PL) intensity. Fig. 4(a,b) shows the photoluminescence of the mixed-phase tin oxide at various annealing temperatures in rich and poor environments. The PL of commercial SnO_2 was stimulated by a 345 nm laser source. The PL emission exhibited two peaks at approximately 480 nm (2.60 eV) and 525 nm (2.36 eV), which are attributed to oxygen vacancies and lattice distortion in SnO_2 [33, 34]. The intensities of the photoluminescence spectrum of the tin oxides depended on the annealing temperature. In a general crystalline oxide system, the PL intensity decreased with increasing annealing temperature due to the reduction of surface defects, which are related to the emission center. In contrast, the as-prepared powder in this work was amorphous, containing numerous oxygen vacancies and disordered bound hydroxyl groups (OH^-), which acted as non-radiative centers and suppressed the PL emission. Upon annealing, these defects and disorder states were passivated, resulting in a more ordered structure. Furthermore, the amorphous tin oxides were induced to form intermediate Sn_2O_3 and Sn_3O_4 phases alongside the SnO_2 phase by thermal energy. Consequently, the PL intensity of defect SnO_2 increased with annealing temperature under both air and N_2 conditions [35, 36], which acted as non-radiative centers and suppressed the PL emission. Upon annealing, these hydroxyl groups, defects, and disorder states were passivated, resulting in a more ordered structure. Furthermore, the amorphous tin oxides were induced to form intermediate Sn_2O_3 and Sn_3O_4 phases alongside the SnO_2 phase by thermal energy. Therefore, the PL intensity of defect SnO_2 increased with annealing temperature under both air and N_2 conditions. The PL spectra of 500 °C powder in an air environment showed the highest intensity, comparable to the PL signal from a commercial SnO_2, confirming the dominance of SnO_2 vacancies. Nevertheless, the PL intensity of the 100 °C powder in both conditions exhibited a silent peak due to the amorphous properties of the tin oxides. Moreover, the intensity of the PL corresponded to the recombination rate of the electrons and holes. Hence, the 100 °C and the prepared powder were more suitable for photocatalytic activity, which favors the low recombination rate [28].

For an in-depth investigation of the mixed-phase tin oxide phase evolution, Raman spectroscopy was used to demonstrate the phase transformation of the mixed-phase amorphous tin oxides, as shown in Fig. 5, Fig. S3, and Fig. S4. The Raman spectra of as-prepared powder and the 100 °C to 200 °C powder under both conditions demonstrated the Raman vibration modes of B_{1g} and A_{1g} at ∼113, 200 cm^{-1} of SnO, and the broad peak from 370 to 800 cm^{-1} was deconvoluted into five peaks around ∼374, 453, 538, 625, and 704 cm^{-1}, which were correlated with vibration modes of A_{2g}, E_g, S_1, A_{1g}, A_{2u} of SnO_2. However, in the N_2 environment, the vibration modes of Sn_2O_3 and Sn_3O_4 could be observed starting from the temperature of 200 °C. In the experiments, the as-prepared powder exhibited a mixed phase of SnO and SnO_2, which contained residual OH^- groups within the tin oxide structure, as indicated by the S_1 peak in the Raman spectrum and the O_3 peak in the XPS spectrum (Fig. 2(d,f)). This suggested that hydroxyl groups were embedded within the tin oxide network. During annealing in N_2 at 200 °C, these OH^- groups were partially removed. However, the limited amount of oxygen in N_2 led to the formation of vacancies that could not be fully compensated and might lead to the disproportion between Sn^{2+} (SnO) and Sn^{4+} (SnO_2) [37, 38], facilitating in the formation of intermediate phases, such as Sn_2O_3 and Sn_3O_4, which could be interpreted as oxygen deficient of SnO_2 in the plane of (1 0 1) as confirmed by the Raman vibration at ∼139 and 168 cm^{-1} [31, 32]. In contrast, the presence of sufficient oxygen conditions was available to fill these vacancies, which delayed the formation of the intermediate phase at lower annealing temperatures in an air condition. At higher annealing temperatures (⩾300 °C), the increase in thermal energy could enhance the reaction between SnO and oxygen and SnO_2 [39, 40]. Additionally, the residual OH^- groups were released more rapidly and could not be replenished with sufficient oxygen, leading to the formation of Sn_2O_3 or Sn_3O_4 within the system. Additionally, at 300 °C and 400 °C in an air environment, the Raman vibration modes B_{1g} and A_{1g} of SnO exhibited an increase in intensity, which could be attributed to the thermal decomposition of intermediate tin-hydroxyl species into SnO. Moreover, the vibration of SnO_2 exhibited a higher peak at ∼636 (A_{1g}) and 789 cm^{-1} (B_{2g}) than at the 50 °C and 200 °C conditions, corresponding to the rearranged atoms of SnO_2 with the pattern and a more significant number of SnO_2 formation by combining SnO, Sn_2O_3, and Sn_3O_4 with oxygen. Furthermore, the tin-hydroxyl precursors could be transformed into SnO_2 through thermal annealing. Therefore, it agrees with the board peaks of rutile SnO_2 that were observed in the XRD pattern. In the air environment, the powder at 500 °C demonstrated the peaks without the vibration modes of SnO. So, the most SnO reacted with oxygen and completely transformed to Sn_2O_3, Sn_3O_4, and SnO_2 due to the appropriate amount of oxygen and thermal energy, as shown in Fig. 6(a). In contrast, the 500 °C powder in N_2 exhibited the vibration mode of SnO, from the lack of oxygen, which led to the incomplete transformation to a higher oxidation state of SnO_2, as shown in Fig. 6(b). The phase evolution conclusion of mixed-phase amorphous tin oxides is summarized in Table 1 and Fig. 7. It should be noted that the p-SnO phase could be observed in all conditions except at 500 °C in air.

CONCLUSION

The mixed-phase amorphous tin oxide micro and nanoparticles could be successfully synthesized via an electrochemical process, exhibiting a porous morphology. The XRD analysis revealed broad signals, confirming the amorphous properties of the as-prepared tin oxide and after annealing at temperatures ranging from 100 °C to 200 °C in air and N_2. In contrast, annealing at 300 °C to 500 °C revealed the crystalline nature, dominated by SnO_2 peaks. The PL spectra indicated an increased degree of oxygen vacancies in SnO_2 depending on the annealing temperatures. However, the characterizations by XRD alone were insufficient to reveal the phase evolution, whereas Raman spectroscopy effectively revealed the phase evolution of the mixed-phase amorphous tin oxides. The results indicated that the amorphous tin oxides (SnO and SnO_2) could be transformed into SnO, Sn_2O_3, Sn_3O_4, and SnO_2 at 300 to 400 °C by the reaction of SnO and oxygen and SnO_2. Furthermore, the amorphous tin oxides could evolve into n-type of Sn_2O_3, Sn_3O_4, and SnO_2 in an air environment at 500 °C. In the N_2 environment, the deficiency of oxygen led to the 200 °C tin oxides being transformed faster into SnO, Sn_2O_3, Sn_3O_4, and SnO_2 than in sufficient oxygen conditions. Moreover, the p-SnO phase could be observed in all conditions except at 500 °C in air. These findings highlighted the pivotal role of Raman spectroscopy in resolving subtle phase transitions and provided essential guidelines for tailoring hybrid amorphous tin oxide phases to achieve optimized performance in p–n junction devices.

Appendix A. Supplementary data

Supplementary data associated with this article can be found at https://dx.doi.org/10.2306/scienceasia1513-1874.2025.s024.

Acknowledgements: This research was partially supported by Chiang Mai University. Suparoek Yarin would like to acknowledge the financial support from SAST and the Graduate School, Chiang Mai University.

REFERENCES

1. Bhattacharjee A, Ahmaruzzaman M (2015) A green approach for the synthesis of SnO_2 nanoparticles and its application in the reduction of p-nitrophenol. *Mater Lett* **157**, 260–264.
2. Ren Q, Zhang X, Wang Y, Xu M, Wang J, Tian Q, Jia K, Liu X, et al (2021) Shape-controlled and stable hollow frame structures of SnO and their highly sensitive NO_2 gas sensing. *Sens Actuators B* **340**, 129940.
3. Khumaeni A, Istanti T, Hidayanto E, Nurhasanah I (2022) Characteristics of tin oxide nanoparticles produced by pulsed laser ablation technique in various concentrations of chitosan liquid and their potential application as an antibacterial agent. *Results Eng* **16**, 100742.
4. Wu P, Wang S, Li X, Zhang F (2021) Advances in SnO_2-based perovskite solar cells: from preparation to photovoltaic applications. *J Mater Chem A* **9**, 19554–19588.
5. Santhi K, Rani C, Karuppuchamy S (2016) Synthesis and characterization of a novel SnO/SnO_2 hybrid photocatalyst. *J Alloys Compd* **662**, 102–107.
6. Li L, Zhang C, Chen W (2015) Fabrication of SnO_2-SnO nanocomposites with p–n heterojunctions for the low-temperature sensing of NO_2 gas. *Nanoscale* **7**, 12133–12142.
7. Du W, Wan Z, Zhu J, Liu X, Chen L, Li S, Kang N, Wang C (2024) *In situ* one step growth of amorphous tin oxide electron transport layer for high-performance perovskite solar cells. *RSC Adv* **14**, 12650–12657.
8. Wang J, Li H, Meng S, Ye X, Fu X, Chen S (2017) Controlled synthesis of Sn-based oxides via a hydrothermal method and their visible light photocatalytic performances. *RSC Adv* **7**, 27024–27032.
9. Sadeghzadeh-Attar A, Bafandeh MR (2018) The effect of annealing temperature on the structure and optical properties of well-aligned 1D SnO_2 nanowires synthesized using template-assisted deposition. *CrystEngComm* **20**, 460–469.
10. Guillén C, Herrero J (2019) P-type SnO thin films prepared by reactive sputtering at high deposition rates. *J Mater Sci Technol* **35**, 1706–1711.
11. Cai T, Tursun R, Wu Z, Sun Q (2023) Synthesis and gas sensing properties of amorphous $NiTiO_3$. *ScienceAsia* **49**, 523–528.
12. Han S, Cui L, Li Z, Luan K (2024) High energy storage performance of (1–x)$Ba_{0.9}Ca_{0.1}TiO_3$-x$BaSn_{0.1}Ti_{0.9}O_3$ bulk ceramics. *ScienceAsia* **50**, ID 2024092.
13. Avis C, Kim Y, Jang J (2019) Amorphous tin oxide applied to solution processed thin-film transistors. *Materials* **12**, 3341.
14. Lee K-M, Lee D-J, Ahn H (2004) XRD and TEM studies on tin oxide (II) nanoparticles prepared by inert gas condensation. *Mater Lett* **58**, 3122–3125.
15. Sornadurai D, Sridharan V, Ajikumar PK, Ravindran TR, Subramanian N (2017) One-step solvothermal synthesis of SnO — structural, thermal stability and optical characterizations. *AIP Conf Proc* **1832**, 140049.
16. Khan AF, Mehmood M, Rana AM, Bhatti MT, Mahmood A (2009) Optical characterization of rf-magnetron sputtered nanostructured SnO_2 thin films. *Chin Phys Lett* **26**, 077803.
17. Wang X, Wang X, Di Q, Zhao H, Liang B, Yang J (2017) Mutual effects of fluorine dopant and oxygen vacancies on structural and luminescence characteristics of F-doped SnO_2 nanoparticles. *Materials* **10**, 1398.
18. Azam A, Habib SS, Salah NA, Ahmed F (2013) Microwave-assisted synthesis of SnO_2 nanorods for oxygen gas sensing at room temperature. *Int J Nanomed* **8**, 3875–3881.
19. Mehraj S, Ansari MS, Alimuddin (2015) Annealed SnO_2 thin films: structural, electrical and their magnetic properties. *Thin Solid Films* **589**, 57–65.
20. Mortelliti MJ, Wang AN, Dempsey JL (2019) Atomic layer deposition of SnO_x onto mesoporous, nanocrystalline TiO_2 and SnO_2 thin films. *Polyhedron* **171**, 433–447.
21. Akyil C, Akdas G, Afsin P, Ürgen M (2019) Freestanding SnO_2 films produced with anodic polarization in acidic media containing colloidal tin hydroxides. *Mater Chem Phys* **221**, 263–271.
22. Akgul FA, Gumus C, Er AO, Farha AH, Akgul G, Ufuktepe

Y, Liu Z (2013) Structural and electronic properties of SnO_2. *J Alloys Compd* **579**, 50–56.

23. Lee HB, Kumar N, Ovhal MM, Kim YJ, Song YM, Kang JW (2020) Dopant-free, amorphous–crystalline heterophase SnO_2 electron transport bilayer enables >20% efficiency in triple-cation perovskite solar cells. *Adv Funct Mater* **30**, 2001559.
24. Xing WD, Lee MS, Choi SH (2018) Separation of Ag(I) by ion exchange and cementation from a raffinate containing Ag(I), Ni(II) and Zn(II) and traces of Cu(II) and Sn(II). *Processes* **6**, 112.
25. Tan ZH, Kong XY, Ng BJ, Soo HS, Mohamed AR, Chai SP (2023) Recent advances in defect-engineered transition metal dichalcogenides for enhanced electrocatalytic hydrogen evolution: perfecting imperfections. *ACS Omega* **8**, 1851–1863.
26. Ullah H, Usman F, Rasheed MA, Khan AA, Ahmad R, Lee SY, Heo J, Ali G, et al (2022) Anodic SnO_2 nanoporous channels functionalized with CuO quantum dots for selective H_2O_2 biosensing. *ACS Appl Nano Mater* **5**, 9096–9111.
27. Liu LZ, Wu XL, Gao F, Shen JC, Li TH, Chu PK (2011) Determination of surface oxygen vacancy position in SnO_2 nanocrystals by Raman spectroscopy. *Solid State Commun* **151**, 811–814.
28. Wang Z, Yang C, Lin T, Yin H, Chen P, Wan D, Xu F, Huang F, et al (2013) H-doped black titania with very high solar absorption and excellent photocatalysis enhanced by localized surface plasmon resonance. *Adv Funct Mater* **23**, 5444–5450.
29. Liu Y, Tian L, Tan X, Li X, Chen X (2017) Synthesis, properties, and applications of black titanium dioxide nanomaterials. *Sci Bull* **62**, 431–441.
30. Monshi A, Foroughi MR, Monshi MR (2012) Modified Scherrer equation to estimate more accurately nanocrystallite size using XRD. *World J Nano Sci Eng* **2**, 154–160.
31. Balgude SD, Sethi YA, Kale BB, Munirathnam NR, Amalnerkar DP, Adhyapak PV (2016) Nanostructured layered Sn_3O_4 for hydrogen production and dye degradation under sunlight. *RSC Adv* **6**, 95663–95669.
32. Li S, Qin F, Peng Q, Liu S, Zhang Z, Zhang D, Liu C, Li D, et al (2020) Van der Waals mixed valence tin oxides for perovskite solar cells as UV-stable electron transport materials. *Nano Lett* **20**, 8178–8184.
33. Sial MAZG, Iqbal M, Siddique Z, Nadeem MA, Ishaq M, Iqbal A (2017) Synthesis and time-resolved photoluminescence of SnO_2 nanorods. *J Mol Struct* **1144**, 355–359.
34. Bhatnagar M, Kaushik V, Kaushal A, Singh M, Mehta BR (2016) Structural and photoluminescence properties of tin oxide and tin oxide: C core–shell and alloy nanoparticles synthesised using gas phase technique. *AIP Adv* **6**, 095321.
35. Mulder JT, Meijer MS, van Blaaderen JJ, du Fosse I, Jenkinson K, Bals S, Manna L, Houtepen AJ (2023) Understanding and preventing photoluminescence quenching to achieve unity photoluminescence quantum yield in Yb:YLF nanocrystals. *ACS Appl Mater Interfaces* **15**, 3274–3286.
36. Zhu K, Frehan SK, Mul G, Huijser A (2022) Dual role of surface hydroxyl groups in the photodynamics and performance of NiO-based photocathodes. *J Am Chem Soc* **144**, 11010–11018.
37. Yin T, Lee J, Moosavi-Khoonsari E, Jung I-H (2021) Critical evaluation and the thermodynamic optimization of the Sn–O system. *Ceram Int* **47**, 29267–29276.
38. Cahen S, David N, Fiorani JM, Maître A, Vilasi M (2003) Thermodynamic modelling of the O–Sn system. *Thermochim Acta* **403**, 275–285.
39. Campo CM, Rodriguez JE, Ramirez AE (2016) Thermal behaviour of romarchite phase SnO in different atmospheres: a hypothesis about the phase transformation. *Heliyon* **2**, e00112.
40. Moreno MS, Mercader RC, Bibiloni AG (1992) Study of intermediate oxides in SnO thermal decomposition. *J Phys Condens Matter* **4**, 351–355.

Appendix A. Supplementary data

Table S1 Calculation of crystalline grain size based on XRD pattern.

Atmosphere	Temperature (°C)	2θ (°)	hkl	FWHM (rad)	D (nm)
Air	300	52.02	211	0.039	3.95
	400	52.11	211	0.030	5.22
	500	26.42	110	0.022	6.54
		33.80	101	0.013	10.76
		51.87	211	0.017	9.31
N_2	300	52.21	211	0.033	4.71
	400	26.48	110	0.024	5.94
		33.94	101	0.024	6.16
		52.09	211	0.027	5.69
	500	26.50	110	0.016	8.74
		33.83	101	0.015	9.71
		51.89	211	0.015	9.99

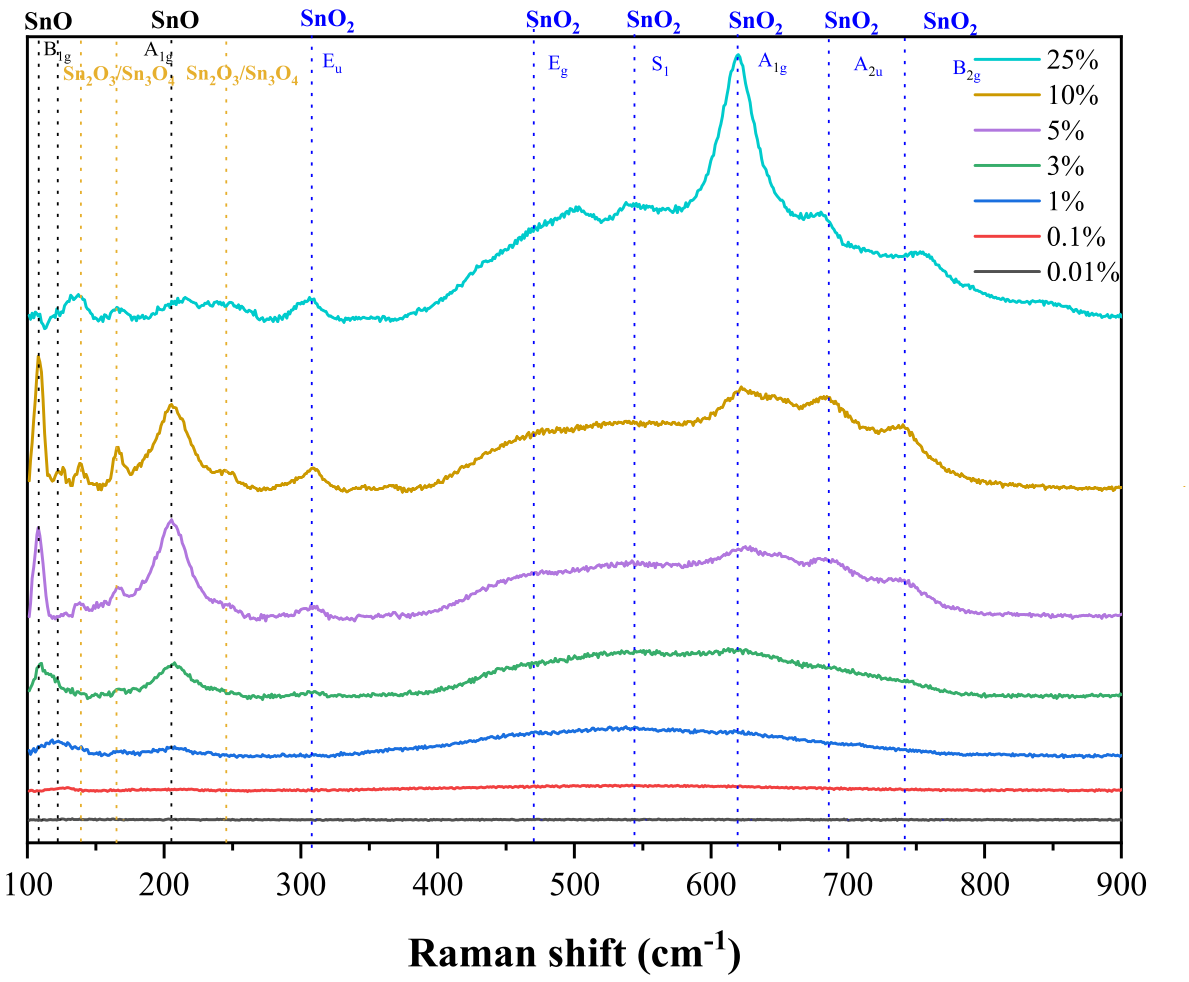

Fig. S1 The Raman spectra of as-prepared tin oxides micro/nanoparticles in different laser intensities from 0.01% to 25%.

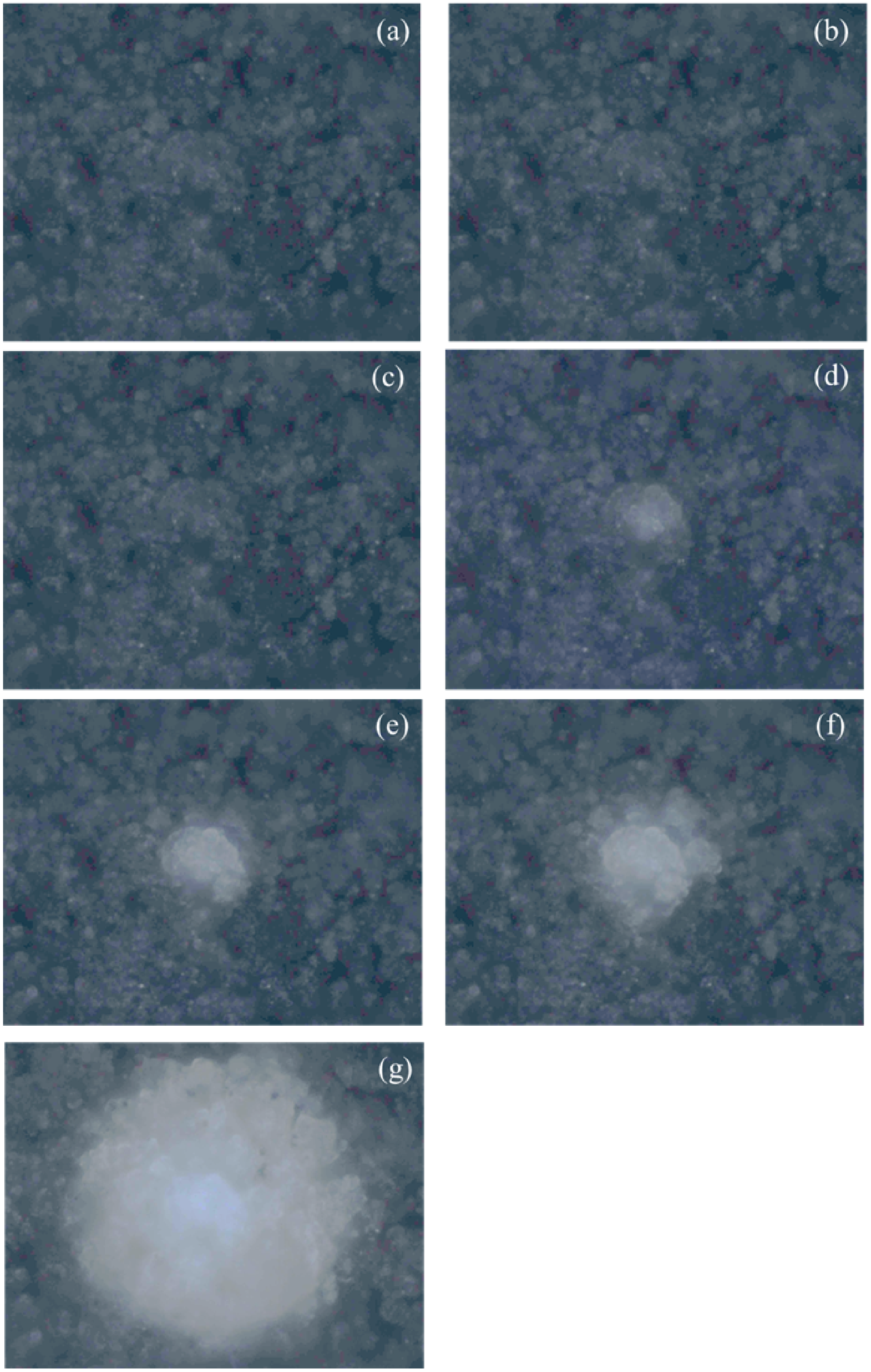

Fig. S2 The photograph of as-prepared tin oxides micro/nanoparticles in different laser intensities (0.01% (a), 0.1% (b), 1% (c), 3% (d), 5% (e), 10% (f), and 25% (g)).

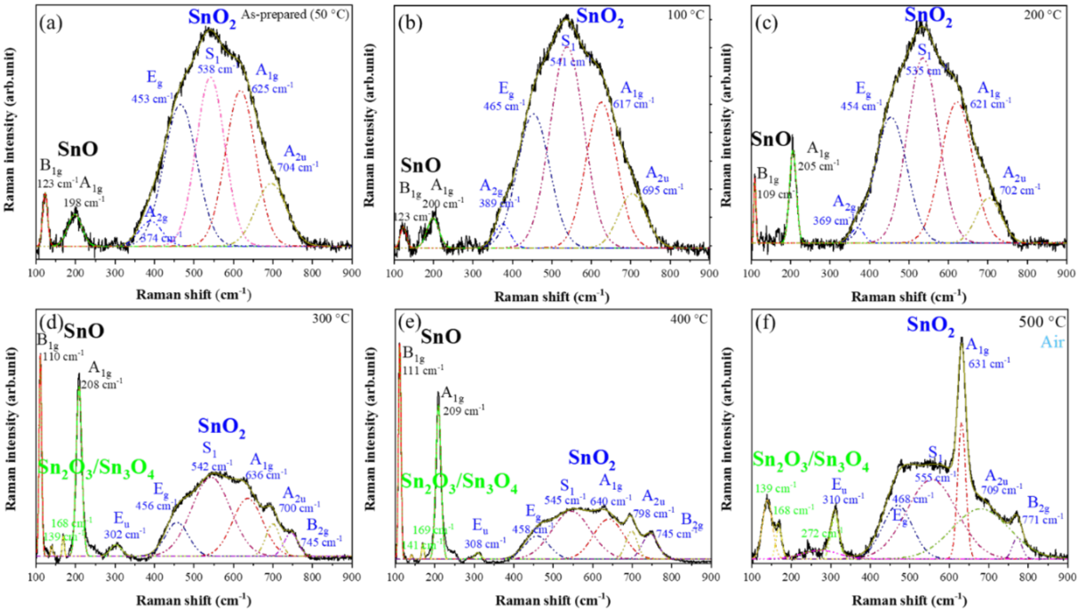

Fig. S3 Gaussian deconvoluted Raman spectra of tin oxide micro/nanoparticles in different annealing temperatures in the air environment (as-prepared 50 °C (a), 100 °C (b), 200 °C (c), 300 °C (d), 400 °C (e), and 500 °C (f)).

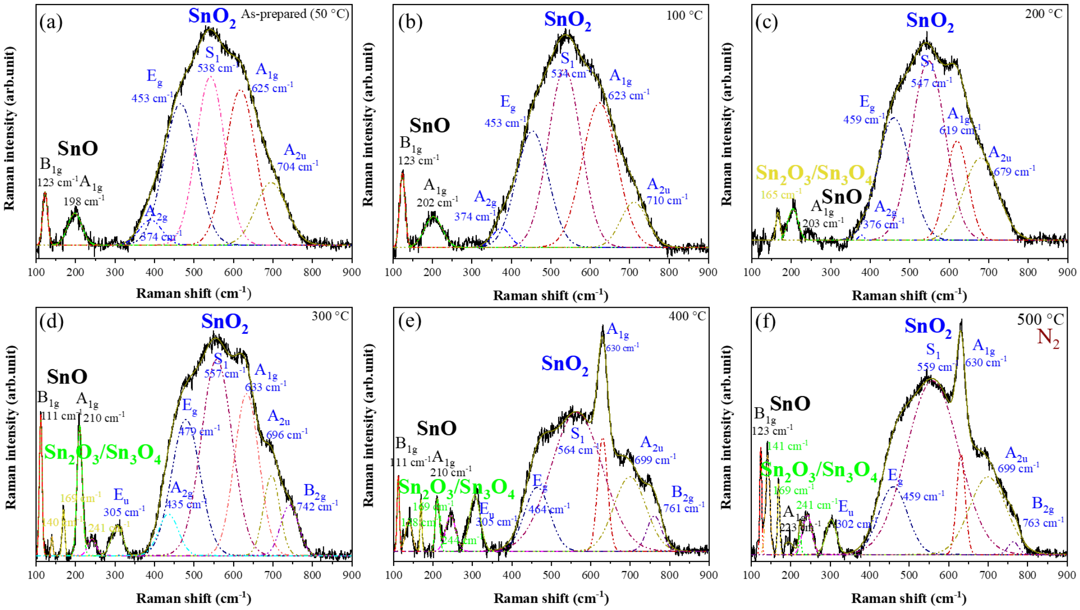

Fig. S4 Gaussian deconvoluted Raman spectra of tin oxide micro/nanoparticles in different annealing temperatures in N_2 environment (as-prepared 50 °C (a), 100 °C (b), 200 °C (c), 300 °C (d), 400 °C (e), and 500 °C (f)).